

SyncTwin: Fast Digital Twin Construction and Synchronization for Safe Robotic Manipulation

Ruopeng Huang^{1,2}, Boyu Yang², Wenlong Gui², Jeremy Morgan², Erdem Biyik², and Jiachen Li^{1*}

¹University of California, Riverside ²University of Southern California

*Corresponding author

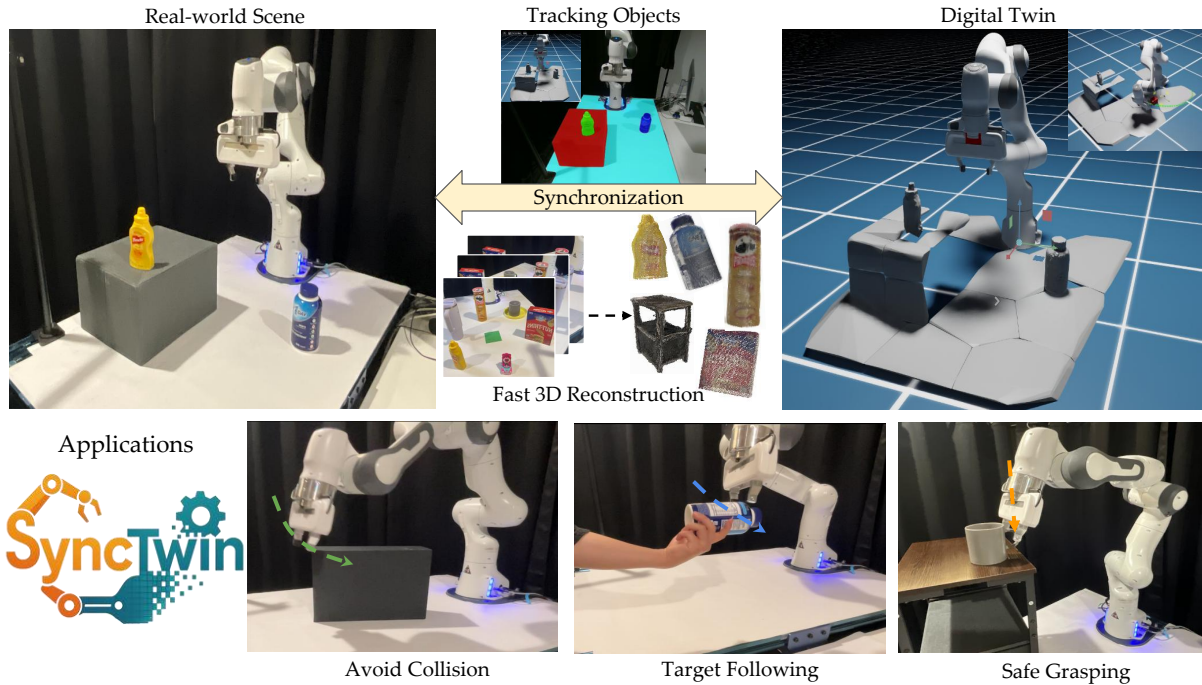


Fig. 1: SyncTwin is a system that enables fast digital twin construction and real-time synchronization through efficient 3D scene reconstruction and object tracking. By bridging motion planning between simulation and the real world, the system supports dynamic obstacle avoidance, target following, and safe grasping under single-view occlusion in real-world environments.

Abstract—Accurate and safe robotic manipulation under dynamic and visually occluded conditions remains a core challenge in real-world deployment. We introduce SyncTwin, a novel digital twin framework that unifies fast 3D scene reconstruction and real-to-sim synchronization for robust and safety-aware robotic manipulation in such environments. In the offline stage, we employ VGGT to rapidly reconstruct object-level 3D assets from RGB images, forming a reusable geometry library. During execution, SyncTwin continuously synchronizes the digital twin by tracking real-world object states via point cloud segmentation updates and aligning them through colored-ICP registration. The synchronized twin enables motion planners to compute collision-free and dynamically feasible trajectories in simulation, which are safely executed on the real robot through a closed real-to-sim-to-real loop. Experiments in dynamic and occluded scenes show that SyncTwin improves manipulation performance and motion safety, demonstrating the effectiveness of digital twin synchronization for real-world robotic execution. The video demos and code can be found on the project website: <https://sync-twin.github.io/>.

I. INTRODUCTION

Achieving accurate and safe robotic manipulation in dynamic real-world environments remains a long-standing challenge due to incomplete perception and scene dynamics. Without an accurate understanding of their surroundings, robots risk colliding with the environment, which may damage hardware or even endanger humans [1]. Thus, both in real-robot online training and in real-world robot model deployment, enabling robots to safely plan and execute motions under dynamic scene changes is a critical concern. Unlike simulation, where complete scene geometry and object states are fully accessible, real-world perception often provides only partial and occluded observations. As a result, although many motion-planning algorithms [2, 3, 4] demonstrate strong performance in simulation, robust motion planning in real-world environments remains an open problem with significant challenges.

Several recent efforts have attempted to bridge the gap between perception and control. Voxel-based mapping systems like NVBlox [5] enable online obstacle reconstruction, yet they only provide a voxel grid, which is a representation too coarse for reliable manipulation. End-to-end reactive policies like DRP [6] handle dynamics through continuous control but require robot-specific retraining and lack generalization across new hardware or environments. And both share a critical limitation: they operate without a consistent and complete model of the scene, leading to unsafe or unreliable executions.

Bridging this gap between simulation and the real world, a robot needs a perception model that can efficiently perceive what objects exist in the environment and also track how the real-world scene evolves over time. In other words, instead of planning in a static or outdated simulation, the robot should plan within a dynamic digital twin that mirrors the physical world in real time, where perception and control are tightly coupled through continuous real-to-sim synchronization. However, real-world perception is inherently partial: single-view occlusions often reveal only fragments of object geometry, making grasping and motion planning unreliable. Inspired by SAM4D [7], which maintains a memory bank of object assets, we incorporate the idea of leveraging object-level memories to complete partial observations at execution time. We develop **SyncTwin**, a digital twin framework equipped with an object memory bank that performs real-time object tracking from point clouds, injects accurate poses and geometries into simulation, and closes the loop by executing planned trajectories back on the real robot, addressing a key limitation of prior digital twin systems, which do not support continuous real-to-sim-to-real synchronization, as illustrated in Fig. 1.

SyncTwin operates in two stages. In Stage I, VGGT [8] generates scene-level point clouds from RGB inputs. Object-level point clouds are extracted via projection, segmentation, and denoising, then converted into lightweight meshes and stored in a memory bank. In Stage II, the digital twin is continuously synchronized with the real world through online object tracking and GPU-accelerated colored-ICP [9]. Combined, these two methods align partial observations with stored assets to maintain a consistent and complete scene representation. The updated digital twin is streamed into Isaac Sim [10], allowing cuRobo [11] to perform motion planning and generate collision-aware trajectories. Moreover, this architecture can be transferred to different real robots without any retraining.

The main contributions of this paper are as follows:

- We present the first digital twin framework that tracks 3D objects in real time from point clouds and updates their poses and geometries in a synchronized simulation, enabling collision-aware planning and a closed real-to-sim-to-real loop for dynamic, partially observed scenes.
- We introduce a fast, low-cost RGB-only method that constructs 3D geometry assets using learning-based geometry estimation and projection-based segmentation.
- We develop a real-time 3D segmentation and tracking module that processes streaming RGB-D camera data.
- Our experiments demonstrate that the proposed system

improves grasp accuracy and safety in single-view and occluded settings, while also achieving state-of-the-art efficiency in 3D geometry asset reconstruction.

II. RELATED WORK

3D Scene Reconstruction and Segmentation. Traditional 3D scene reconstruction approaches rely on RGB-D input from depth sensors to estimate geometry [12, 13, 14, 15]. More recent approaches operate purely on RGB images, either through optimization-based pipelines such as Structure-from-Motion (SfM) [16, 17, 18, 19] and Multi-View Stereo (MVS) [20, 21, 22], or through learning-based frameworks such as MVSNNet [23], NeRF [24], and 3D Gaussian Splatting [25]. While these methods can recover visually plausible geometry, they often require substantial computation time to produce complete reconstructions. For robotics applications, object-centric 3D segmentation is important as well. Prior work has explored segmentation directly on point clouds using learned clustering and aggregation strategies [26, 27, 28], as well as multi-view projection of 2D masks for 3D instance segmentation [29, 30, 31]. However, projection-based methods typically require accurate camera extrinsics [32, 33], and little research has examined how such strategies perform when applied to point clouds produced by learning-based reconstruction methods. Our work addresses this gap by unifying learned 3D reconstruction with mask-guided multi-view segmentation to achieve efficient and robust object asset generation, providing geometry-aware perception to support safe and reliable motion planning in robotic manipulation.

Digital Twin for Robotic Manipulation. Digital twin systems have become increasingly popular for sim-to-real transfer, particularly in training reinforcement learning and imitation learning policies [34, 35, 36, 37]. And several studies leverage generated digital twins as a form of data augmentation to enhance the generalization of downstream models [38, 39]. However, existing frameworks typically reconstruct static scenes once before training [40] and do not maintain continuous synchronization with the evolving physical world. Some recent efforts attempt real-time tracking by detecting object locations with 2D detectors [41], but they often lack precise pose estimation or geometry updates. In contrast, our system enables continuous synchronization of the digital twin with real-world online perception, which enables accurate tracking and reliable manipulation in dynamic environments under occlusion.

Safe Motion Planning for Manipulation. Safe and robust motion planning remains a critical challenge for robotic manipulation in unstructured environments [42, 43]. Classical and learning-based planners [2, 3, 4] typically operate in simulation, where the environment is fully accessible. When deployed in the real world, however, they must handle partial observations. To narrow this gap, several methods construct static point cloud maps and import them into simulation for offline planning [44], though such maps struggle to support real-time adaptation. Other approaches aim to ensure safety by predicting collision-free actions directly from images in latent space [45, 46], using force-sensing-based control [47, 48], or

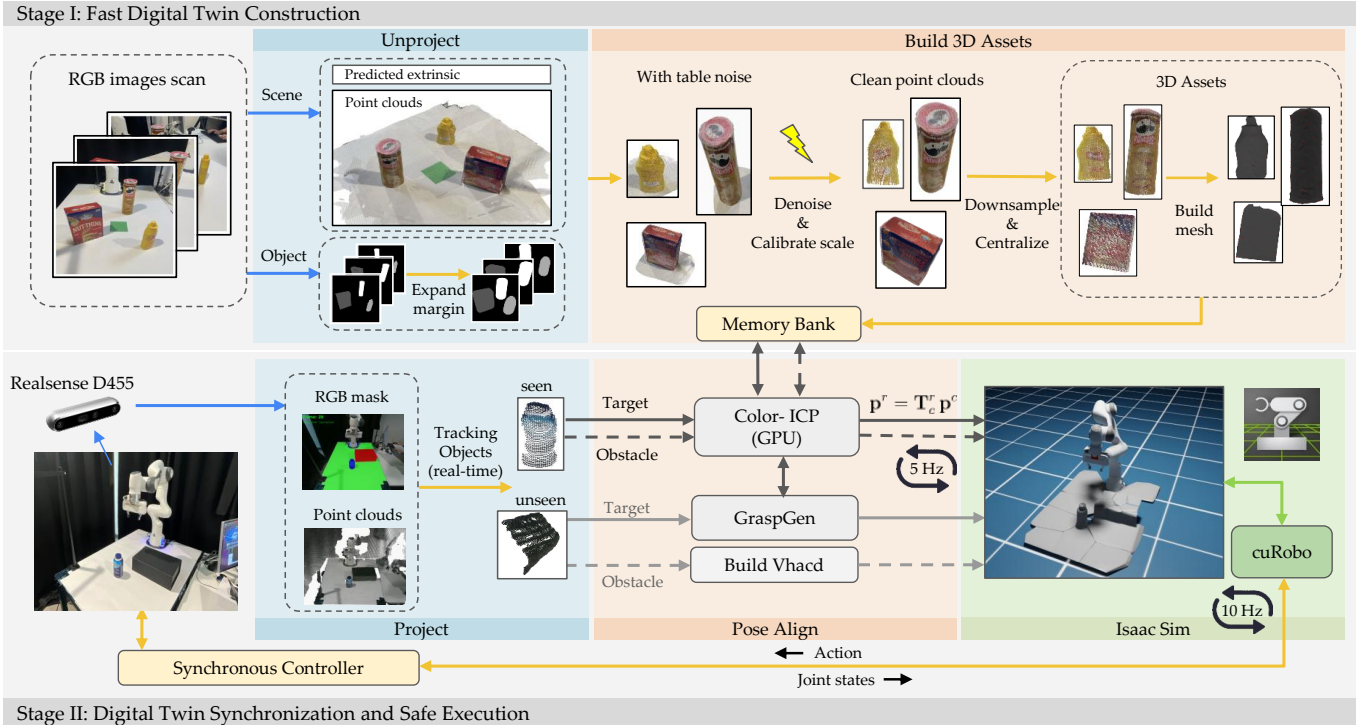


Fig. 2: **Framework of the SyncTwin.** Stage I constructs simulation-ready 3D assets from RGB images using VGGT. Multi-view masks are unprojected into point clouds, then denoised, scaled, and meshed into clean object assets stored in the memory bank. Stage II performs real-time object segmentation, pose tracking, and asset-based completion, enabling grasp generation and reactive motion planning in a closed real2sim2real loop. By continuously updating the digital twin and leveraging simulation for decision making, the system ensures safe and adaptive execution under dynamic and partially occluded environments.

distilling planning policies from point cloud observations [49, 6, 50]. NVBlox improves online safety by voxelizing scene geometry and segmenting the robot in real time [5]. In contrast, our method maintains a dynamically synchronized digital twin that continuously provides updated scene geometry to the planner, enabling safe execution in dynamic environments.

III. METHOD

SyncTwin consists of two stages: (1) fast digital twin construction and (2) digital twin synchronization. An overall framework of the proposed method is provided in Fig 2.

A. Problem Formulation

We aim to enable safe robotic manipulation in dynamic, partially observable real-world environments by maintaining a *continuously synchronized digital twin*. This problem can be decomposed into the following components:

Stage I: Fast Digital Twin Construction. Given a small set of RGB images $\{\mathbf{I}_i\}_{i=1}^N$ along with intrinsics K and estimated extrinsics $\{\mathbf{T}_i^{\text{world}}\}_{i=1}^N$. Our goal is to generate object-level, simulation-ready 3D assets $\mathbb{B} = \{\mathcal{X}_j, \mathcal{M}_j^{3D}\}$ from these images. The main challenge is that learning-based extrinsics contain unstable errors, causing mask-projection misalignment and table-object mixing in the reconstructed point cloud, which must be addressed to obtain clean object geometry.

Stage II: Online Digital Twin Synchronization. During execution, the fixed calibrated camera receives streaming RGB-D frames and corresponding partial point clouds \mathcal{X}_p . The objective is to maintain accurate object poses $\mathbf{T}_j^{\text{world}}$ in the simulator by aligning \mathcal{X}_p with their complete assets $\mathcal{X}_m \in \mathbb{B}$. This synchronized scene is streamed into Isaac Sim [10], where cuRobo’s MPC planner [11] produces short-horizon, collision-free trajectories $\mathbf{A}_{t:t+H} = \{\mathbf{a}_0, \dots, \mathbf{a}_H\}$. The key challenge is robustly tracking objects under occlusion and partial observation, while ensuring that the object poses and geometries can be accurately updated into the simulator to enable safe real-to-sim-to-real planning and execution.

B. Fast Digital Twin Construction

The first stage aims to rapidly reconstruct the 3D environment and extract object-level representations suitable for real-time simulation, where the focus is to achieve accurate geometric perception for motion planning, rather than photo-realistic reconstruction. We employ VGGT [8] to reconstruct dense scene point clouds directly from a small number of RGB images, which enables efficient extraction of object-level geometry in a fast and low-cost manner without relying on multiple depth sensors or multi-view optimization, while avoiding repeated calibration of the Realsense’s extrinsic.

Nevertheless, there are two major practical challenges. First, the camera extrinsics estimated by VGGT are often inaccurate, which leads to projection misalignment during mask-based

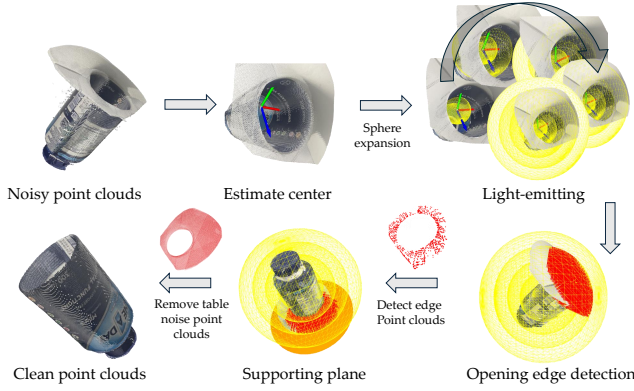


Fig. 3: **Supporting-plane noise removal mechanism.** A virtual light sphere expands from the object center to identify openings and boundary points, enabling filtering of table noise.

segmentation. Second, the generated point cloud is not in a true metric world scale, causing the imported assets to appear incorrectly sized relative to the robot in the simulator. Therefore, Stage I focuses on producing simulation-ready 3D digital assets from VGGT outputs by addressing these limitations. We design a four-step pipeline that solves extrinsic inaccuracies, scale consistency, and generates clean object meshes suitable for planning, which is introduced as follows.

Mask Projection Expansion. To mitigate inaccuracies in VGGT-estimated camera extrinsics, each 2D segmentation mask \mathcal{S}_i is spatially expanded before projection, which ensures full coverage of object boundaries and prevents missing edge regions. While mask expansion compensates for projection drift, it also introduces floating outliers (e.g., background points around the object) and merged support-plane regions (e.g., table surfaces). To address this, we apply our point clouds denoising mechanism to isolate the true object shape.

Point Clouds Denoising. Detecting openings or cavities in 3D point clouds is a fundamental step in shape understanding for denoising table noise. We propose a purely geometric method that progressively expands a virtual light sphere from the object’s center and tracks uncovered regions on the spherical sampling space. The algorithm automatically detects openings and extracts rim points around their boundaries without manual boundary selection. Fig. 3 shows the overall process.

Given a point cloud \mathcal{P} , we first estimate a geometric center $\mathbf{c} = \text{mean}(\mathcal{P})$. We then discretize the unit sphere into F directions $\{\mathbf{d}_i\}_{i=1}^F$ using a Fibonacci spiral distribution [51], forming a uniform sampling domain \mathcal{D} . Each point \mathbf{p}_i defines a normalized direction $\hat{\mathbf{v}}_i = (\mathbf{p}_i - \mathbf{c}) / \|\mathbf{p}_i - \mathbf{c}\|$ and is assigned to its nearest angular bucket direction \mathbf{d}_j if $\hat{\mathbf{v}}_i \cdot \mathbf{d}_j \geq \cos(\theta_{\text{tolerance}})$. We then iteratively expand a virtual sphere centered at \mathbf{c} with radius r_t , along the sampled directions.

$$r_{t+1} = r_t + \Delta r, \quad r_{\min}(j) = \min_{i \in \text{bucket } j} \|\mathbf{p}_i - \mathbf{c}\|. \quad (1)$$

A direction \mathbf{d}_j is marked as *hit* once any assigned point enters the sphere, and unhit directions form a binary mask \mathcal{U}_t . The largest unhit connected component is identified as an

opening or cavity after iterations. We denote by $\mathcal{N}(j) = \{k \mid (j, k) \in \mathcal{P}\}$ the neighborhood of bucket j . Boundary buckets are defined as unhit directions adjacent to hit ones:

$$\mathcal{B} = \{j \in \mathcal{U} \mid \exists k \in \mathcal{N}(j), \text{hit}(k) = 1\}. \quad (2)$$

For each boundary \mathbf{d}_j , the farthest point within tolerance is chosen as a rim sample \mathbf{p}_j^* . Connected components on the spherical adjacency graph are extracted to identify large uncovered regions. Let $\{\mathcal{C}_m\}$ denote all connected components of the unhit set \mathcal{U}_t , \mathcal{C}_{\max} is the largest connected region. The principal opening direction is then computed by averaging the largest unhit component: $\mathbf{n}_{\text{open}} = \frac{\sum_{j \in \mathcal{C}_{\max}} \mathbf{d}_j}{\|\sum_{j \in \mathcal{C}_{\max}} \mathbf{d}_j\|}$. Finally, the rim points $\{\mathbf{p}_j^*\}$ are fitted with a plane using SVD [52] to remove the supporting surface noise points. Compared with RANSAC plane fitting [53], which can only segment dominant planes, our method can detect cavity openings, enabling the identification of ring-shaped planes surrounding the opening.

Real-World Scale Alignment. Since VGGT produces point clouds that are not in a world-scale metric, we estimate a global scale factor to align the reconstructions with world coordinates. Even with known intrinsic parameters, according to the pinhole camera model, monocular geometry cannot determine absolute scale [19]. Therefore, we calibrate the scale using a marker of known physical dimensions within the scene. Implementation details are provided in the Appendix.

Mesh Simplification. To maintain real-time performance in the digital twin, we apply an adaptive mesh decimation that reduces vertex count while preserving geometric fidelity. To avoid over-smoothing across sharp edges, we use an angle-based gating weight $w_{ij} = 1$ if $\theta_{ij} \leq \theta_{\text{th}}$ and 0 otherwise, where θ_{th} is a feature threshold (e.g., 30°) and $\theta_{ij} = \arccos(\mathbf{n}_i^T \mathbf{n}_j)$ for all $j \in \mathcal{N}(i)$. Each vertex is then updated via a selective Laplacian step [54]. Compared to uniform mesh decimation, this feature-aware smoothing preserves sharp edges around handles and object rims, which are critical for accurate grasp planning. All processed point clouds, meshes, and their id are stored in a memory bank, which serves for scene synchronization in Stage II.

C. Online Digital Twin Synchronization

The second stage of our system focuses on real-time object tracking and safe grasp execution through continuous perception, planning synchronization between the real and digital environments. This stage consists of four integrated modules: real-time point cloud segmentation, GPU-accelerated colored-ICP registration, grasp pose generation from complete object models, and dynamic motion planning with cuRobo MPC.

Real-time Point Clouds Segmentation. To achieve real-time segmentation on incoming RGB-D streams, we build a module shown in Fig. 4, that performs continuous inference on camera frames and outputs segmentation masks \mathcal{S}_p , and then projects the mask onto the full point cloud to obtain the corresponding partial object point clouds \mathcal{X}_p . To support streaming input, we design a sliding-window inference mechanism that maintains temporal consistency of object masks across frames, enabling

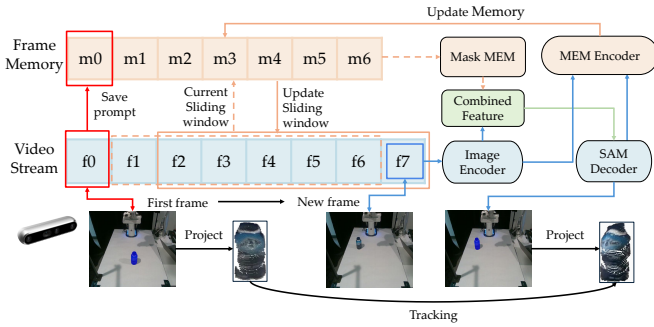


Fig. 4: **Overview of the camera predictor module.** The red solid line indicates that the first frame is persistently stored in the frame memory. The yellow dashed line represents saving frames from the previous time step into memory. The blue and green solid lines denote the data flow and processing of the current frame. Together, the sliding-window mechanism enables real-time video segmentation and object-level point cloud tracking with temporally consistent memory updates.

continuous 3D segmentation and tracking under occlusions. At image size 640×480, our method runs at 15 Hz on RTX 4090.

Colored-ICP Registration. For aligning partial point clouds \mathcal{X}_p obtained from the camera with the corresponding full object model \mathcal{X}_m stored in the memory bank, we employ a colored-ICP algorithm [55] implemented on the GPU via the cupoch library [9]. Unlike traditional geometric ICP, colored-ICP jointly minimizes geometric and color residuals: $E(R, t) = \sum_i [\lambda_g \|R\mathbf{x}_i + t - \mathbf{y}_i\|^2 + \lambda_c \|I(\mathbf{x}_i) - I(\mathbf{y}_i)\|^2]$. Here, (R, t) denotes the rigid transformation between \mathcal{X}_p and \mathcal{X}_m , and $I(\cdot)$ represents point color intensity. The weighting factors λ_g and λ_c balance geometric and color terms.

Grasp Pose Generation and Obstacle Representation. For unseen target objects, we directly apply GraspGen to the partial point cloud. In contrast, once a seen target object is registered, we replace its partial observation with the complete point cloud \mathcal{X}_m from the memory bank and feed it into GraspGen to predict grasp poses $\{\mathbf{T}_{\text{grripper}} = f_{\text{GraspGen}}(\mathcal{X}_m)\}$. This replacement mitigates the uncertainty from occlusion and single-view perception, yielding more stable and accurate grasp pose estimation. For unseen obstacles, we dynamically generate multi-convex hulls (V-HACD [56]) from the segmented point cloud for collision modeling. For known obstacles, the aligned object meshes and poses are directly imported into the digital twin for real-time collision checking.

Motion Planning with Real2sim2real Synchronization. Finally, motion planning and control are performed using cuRobo’s MPC framework. At each control step, the robot’s joint states are synchronized with the digital twin, where cuRobo computes an optimized short-horizon trajectory under real-time collision constraints. Only the first control action $\{\mathbf{a}_0\}$ from the predicted trajectory $\mathbf{A}_{t:t+H} = \{\mathbf{a}_0, \mathbf{a}_1, \dots, \mathbf{a}_H\}$ is executed on the real robot, followed by continuous replanning with environment updates, achieving closed-loop synchronization between simulation and reality.

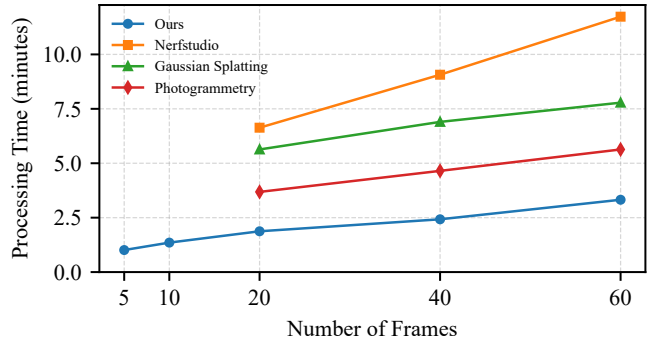


Fig. 5: **Comparison of processing time given different numbers of input images.** The reported time includes both reconstruction and segmentation. In practice, our method achieves reliable reconstruction with as few as 5-10 input images. Results for 5 and 10 images are not reported for the baselines, as they fail to estimate camera extrinsics.

IV. EXPERIMENTS

We evaluate SyncTwin across four dimensions: (1) the efficiency of the fast 3D reconstruction pipeline; (2) the pose accuracy of the synchronized digital twin under both unoccluded and occluded conditions; (3) obstacle avoidance performance under dynamic and single-view occluded conditions; and (4) grasp success rate under single-view occlusion. All experiments are designed to systematically validate both the offline and online components of our framework.

A. Experiment Setup

All experiments are conducted with a Franka Panda robotic arm equipped with an Intel RealSense D455 RGB-D camera mounted above and in front of the workspace. And iPhone 12 for RGB images. We apply voxel-based downsampling to the input point cloud with a voxel size of 3 mm. This is motivated by the fact that the computational complexity of point cloud segmentation algorithms scales linearly with the number of points. The digital twin is implemented in Isaac Sim 4.0 and integrated with the cuRobo MPC motion planning framework, running on a single NVIDIA RTX 4090 GPU. Both perception and planning run on the same GPU, enabling a closed-loop update rate of up to 5 Hz. Motion planning runs at 10 Hz, and the robot’s velocity scaling is set to 0.2. The test objects include bottles, cans, cups, and boxes of various shapes.

B. Baselines and Metrics

Baselines. (1) For *3D reconstruction*: we compare against Photogrammetry [17], NeRF (Nerfstudio [57]), and Gaussian Splatting (3DGS [25]); (2) For *obstacle avoidance*: we adopt NVBlox [5] as the baseline voxel-mapping method. **Ablation Studies.** We analyze performance across the following settings: (1) *Mask Expansion and Denoising*: using variants without mask expansion and without denoising as baselines, evaluating their reconstruction quality against our full segmentation mechanism; (2) *Object Completion*: we use GraspGen [58] as the baseline grasp generator, comparing grasp poses predicted

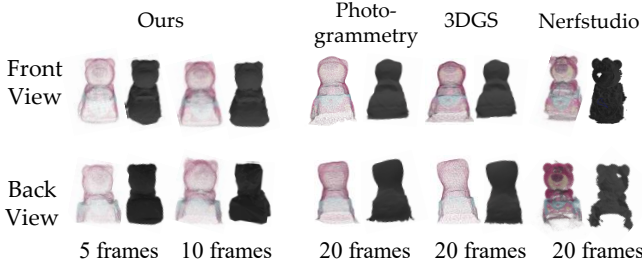


Fig. 6: **Reconstruction comparison given different numbers of input images.** In each column, the left figure shows the point clouds, and the right one shows the untextured mesh.

from single-view partial point clouds (baseline) versus from complete geometry produced by SyncTwin (ours).

Evaluation Metrics. Depending on the experiment, we report the following metrics: reconstruction time (min), dependency on the number of input images N_{\min} , pose accuracy (%), obstacle avoidance rate (%), and grasp success rate (%).

Pose accuracy is evaluated using normalized translation and rotation accuracy scores. For translation, let $\Delta \mathbf{t}_{\text{real}}^{(i)}$ and $\Delta \mathbf{t}_{\text{twin}}^{(i)}$ denote the object translations in the real world and in the digital twin for the i -th trial. The translation error is defined as $e_{\text{trans}}^{(i)} = \left\| \Delta \mathbf{t}_{\text{real}}^{(i)} - \Delta \mathbf{t}_{\text{twin}}^{(i)} \right\|_2$, and the translation accuracy is computed as $\text{Acc}_{\text{trans}} = 1 - \frac{\bar{e}_{\text{trans}}}{t_{\text{real}}}$. For rotation, object orientations are represented as unit quaternions. Given the real and simulated orientations $\mathbf{q}_{\text{real}}^{(i)}$ and $\mathbf{q}_{\text{twin}}^{(i)}$, the angular rotation error is computed as $e_{\text{rot}}^{(i)} = 2 \arccos(|q_{\text{rel}}^w|)$, where $\mathbf{q}_{\text{rel}}^{(i)} = \left(\mathbf{q}_{\text{real}}^{(i)} \right)^{-1} \otimes \mathbf{q}_{\text{twin}}^{(i)}$. The rotation accuracy is defined as $\text{Acc}_{\text{rot}} = 1 - \frac{\bar{e}_{\text{rot}}}{r_{\text{real}}}$. Higher accuracy values indicate better alignment between the digital twin and the real world.

For avoidance tests, we define 3-level outcome levels: FA (full avoidance, no contact with the object, 1.0), EA (edge avoidance, slight contact without displacing the object, 0.8), and CO (collision, noticeable contact that significantly moves the object, 0.0). Weighted success rate:

$$\text{SR} = \frac{N_{\text{FA}} + 0.8 N_{\text{EA}} + 0.0 N_{\text{CO}}}{N} \times 100\%.$$

C. Fast 3D Reconstruction

We evaluate the efficiency and input-image number dependency of SyncTwin’s 3D reconstruction module, comparing against Photogrammetry, 3DGS, and Nerfstudio. Each method reconstructs the same object using 5, 10, 20, 40, and 60 RGB images as input, and all approaches obtain object assets through multi-view projection-based segmentation. The experimental results are summarized as follows for comparison.

Reconstruction Time. As shown in Fig. 5, SyncTwin achieves the shortest reconstruction time across all settings. It generates a simulation-ready mesh in approximately 1-2 minutes using only 5-10 input images, whereas Photogrammetry, 3DGS, and Nerfstudio require more input images and substantially longer processing times, typically ranging from 4 to 8 minutes. As a result, SyncTwin enables significantly faster digital twin construction in new real-world scenarios.

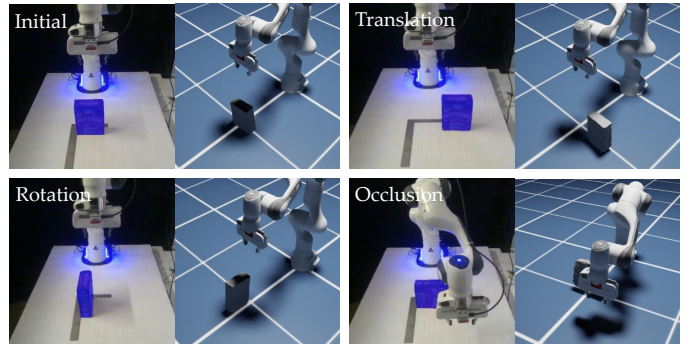


Fig. 7: **Illustration of the pose accuracy evaluation setup.** The left column shows the real-world scene, where the target object (highlighted in blue) is tracked and segmented during object translation, rotation, and occlusion. The right column visualizes the corresponding synchronized digital twin in simulation after object matching and pose alignment.

TABLE I: **Pose accuracy of SyncTwin.** Translation (Trans.) and rotation (Rot.) accuracy are evaluated on different objects under unoccluded and occluded conditions.

Condition	Box		Cup		Bottle		Ketchup	
	Trans.	Rot.	Trans.	Rot.	Trans.	Rot.	Trans.	Rot.
Unoccluded (%)	95.1	78.3	96.3	88.7	94.8	90.4	94.7	82.0
Occluded (%)	85.2	70.4	87.7	78.2	90.3	82.6	91.5	76.3

Dependency on the Number of Input Images. SyncTwin also exhibits the lowest dependency on input-image count. It can generate usable meshes from as few as 5-10 images, whereas competing methods typically require more than 20 images to avoid reconstruction failures caused by unstable camera extrinsic optimization. This low image dependency substantially accelerates asset generation and improves robustness under limited viewpoints, especially because the reported processing time excludes image-capture time, which becomes additional and unpredictable when more images are required.

Furthermore, the qualitative comparison in Fig. 6 shows that our method preserves fine-grained geometric details even with very few input images, as our mesh simplification algorithm effectively maintains high geometric fidelity while reducing the number of mesh vertices, enabling faster simulation performance. For instance, the *bear’s ear shape* remains well preserved with only 5-10 frames, demonstrating both low image dependency and strong geometric consistency.

These properties make SyncTwin a state-of-the-art solution for fast 3D geometry asset generation: the system can construct high-quality, simulation-ready object meshes in about 1 minute, enabling rapid reconstruction of object assets for downstream digital twin synchronization and safe geometry-aware motion planning in real-world environments.

D. Pose Accuracy

We conduct an experiment to evaluate the pose accuracy of the synchronized digital twin. Four object categories (box, cup, bottle, and ketchup bottle) are tested under both unoccluded and single-view occluded conditions. Each object is translated

TABLE II: Comparison of obstacle-avoidance performance between NVBlox and SyncTwin in dynamic environments. Unseen objects (left) are not present in the asset memory, whereas starred objects in the Seen category (right) are stored in the memory bank. SyncTwin achieves significantly higher success rates in both settings, with particularly strong gains when complete object assets are available. Results are reported using the evaluation metrics defined in Sec. IV-B.

Method	Motion	Unseen												Seen (Memory Bank)													
		Box1			Box2			Box3			Box4			SR_unseen (%)	Box1*			Box2*			Box3*			Box4*			SR_seen (%)
		FA	EA	CO	FA	EA	CO	FA	EA	CO	FA	EA	CO		FA	EA	CO										
NVBlox	SelfRot	6	4	10	9	5	6	3	4	13	3	11	6	50.3%	-	-	-	-	-	-	-	-	-	-	-	-	-
	EnterTraj	3	9	8	4	9	7	1	6	13	0	3	17	37.0%	-	-	-	-	-	-	-	-	-	-	-	-	-
SyncTwin	SelfRot	12	7	1	14	5	1	11	7	2	9	9	2	85.5%	18	1	1	16	4	0	15	5	0	13	6	1	93.5%
	EnterTraj	8	8	4	11	6	3	8	7	5	7	8	5	71.5%	12	7	3	12	5	3	10	6	4	9	7	4	78.8%

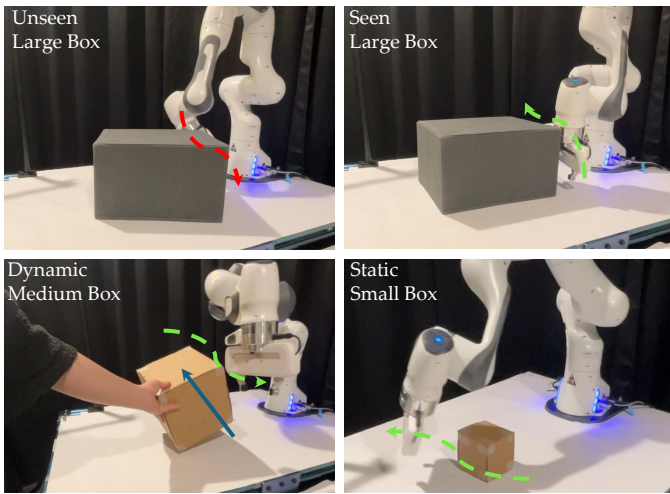


Fig. 8: Examples of SyncTwin’s dynamic obstacle avoidance. Green dashed lines indicate collision-free robot trajectories, while red lines mark trajectories that result in collisions. Blue arrows denote the motion of dynamic obstacles. For unseen objects (top-left), the robot collides with unobserved regions, whereas the same object in the seen case (top-right) is successfully avoided. SyncTwin also handles dynamic obstacles (bottom-left) and small objects (bottom-right) effectively.

by 15 cm along the Cartesian axes and rotated by 90 degrees around the roll, pitch, and yaw axes, with each motion repeated 50 times, as shown in Fig. 7. As shown in Table I, SyncTwin achieves high translation and rotation accuracy across all object categories in the unoccluded setting, with translation accuracy consistently above 90%. Under occlusion, accuracy decreases but remains stable across objects, demonstrating robust pose synchronization under partial observations.

E. Obstacle Avoidance under Occlusion

We adopt the built-in obstacle avoidance benchmark in cuRobo to evaluate the success rate of obstacle avoidance, where the robot repeatedly moves between two target points while avoiding obstacles along its path.

Both NVBlox and SyncTwin are tested on unseen (not stored in the memory bank) obstacles to evaluate avoidance performance. Additionally, SyncTwin is further evaluated on

seen (stored in memory bank) objects recorded in its asset memory to study how prior geometry improves safety and reactivity under single-view occlusion. The experiment tests under two motion patterns: **SelfRot** indicates in-place rotation; **EnterTraj** blocks motion into the predicted trajectory. Each condition is repeated for 20 trials, in total $N = 20 \times 4 = 80$. We test four boxes with sizes of Box1: $10 \times 10 \times 10$ cm, Box2: $20 \times 20 \times 20$ cm, Box3: $10 \times 20 \times 30$ cm, and Box4: $20 \times 22 \times 35$ cm as obstacles. Based on these experimental settings, the results are summarized as follows:

Unseen Object Performance. As shown in Table II, SyncTwin consistently outperforms NVBlox when encountering unseen obstacles under single-view dynamic occlusion. NVBlox exhibits failure modes such as: (1) unstable voxelization for small objects (e.g., Box1) due to sparse depth returns; (2) misclassification of limited height objects (e.g., Box3) as part of the tabletop caused by inconsistent depth estimation; and (3) trajectory intersections when large obstacles (e.g., Box4) fall outside the sensor’s visible region. Across all these cases, SyncTwin maintains markedly higher obstacle-avoidance success rates, demonstrating stronger robustness to object scale, occlusion, and limited viewpoint coverage.

Seen Object Performance. As shown in Table II, SyncTwin achieves further performance improvements when objects are stored in the asset memory. Complete geometric priors obtained in Stage I resolve the challenges posed by small or thin objects, eliminate many failure cases, and convert numerous edge-avoidance cases into full avoidance. These results indicate that SyncTwin not only generalizes better on unseen objects but also achieves substantially higher reliability when the objects have been previously reconstructed, highlighting the importance of SyncTwin’s Stage I memory construction, which enables complete geometric reasoning even under partial observability. Furthermore, Fig. 8 illustrates representative avoidance examples achieved by SyncTwin.

F. Ablation Studies

Mask Expansion and Denoising. Due to inaccurate VGGT-estimated camera extrinsics, multi-view mask projections often become misaligned and fail to fully cover the object. Our ablation study evaluates reconstruction results *w/o mask expansion* and *w/o denoising*. As shown in Fig. 9, removing

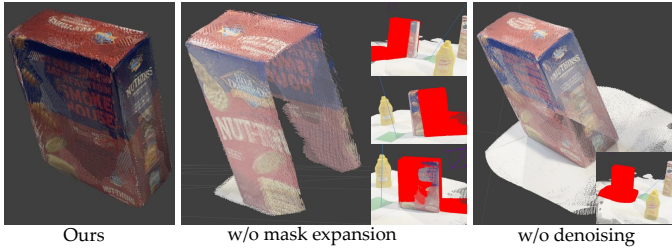


Fig. 9: **Comparison of segmentation-based 3D reconstruction results.** Left: Our method generates a complete and clean object mesh without support-plane noise. Middle: w/o mask expansion, multi-view projections (red) fail to fully overlap, and their intersection leads to missing object geometry. Right: w/o denoising, the intersection of projected regions (red) incorrectly preserves support-plane points, introducing significant noise into the reconstructed point cloud.

TABLE III: **Comparison of grasp success rates before and after geometry completion using GraspGen.** GraspGen is a state-of-the-art point-cloud-based grasp pose generator, and asset-based completion significantly improves its performance across all objects by providing more complete object geometry, resulting in more accurate and safer grasp pose candidates.

Condition	Bottle	Cup (Handle)	Cookie Box	Chips Can
Before Completion (%)	78.3	65.0	81.7	80.0
After Completion (%)	90.0	86.7	93.3	95.0
Improvement	+11.7	+21.7	+11.6	+15.0

margin expansion causes inconsistent projections across view-points, leaving parts of the object missing. Likewise, disabling supporting-plane points denoising preserves table artifacts in the point cloud, resulting in noisy meshes. These comparisons demonstrate that mask expansion and support-plane denoising are essential for obtaining clean 3D assets.

Object Completion. We evaluate the effect of object geometric completeness on grasp generation. When grasp poses are generated from single-view partial point clouds, the limited geometry often leads to incomplete or incorrect grasp configurations. For example, as shown in Fig. 10, the handle of the cup is not perceived, resulting in unsafe or colliding grasps. In contrast, after SyncTwin aligns the observed object with the corresponding complete mesh from the asset library, the grasp generator produces denser, more accurate, and geometrically feasible grasp candidates. This demonstrates that asset-based completion is essential for reliable and collision-free grasp execution in the real world. As shown in Table III, across 60 evaluation trials, grasp success rates increase substantially after geometry completion. The improvement is most pronounced for partially occluded or asymmetric objects, such as the cup with a handle and the chips can, where asset-based completion provides the missing structure needed for reliable planning.

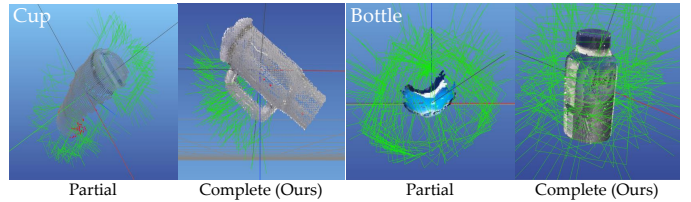


Fig. 10: **Comparison of grasp candidates generated from Ours (w/o Completion) and Ours.** The example objects include a handled cup (left pairs) and a bottle (right pairs). Green lines visualize predicted gripper poses.

G. Discussions

Our work provides a segmentation approach that covers most objects, while some challenging cases remain when applied to learning-based reconstructed point clouds. For instance, the supporting-plane denoising strategy may fail for tall or weakly supported objects such as wine glasses. To the best of our knowledge, this work represents the first attempt to address this problem, and many challenges still remain.

This work emphasizes a principled view of digital twins as real-time synchronization of environmental geometry, rather than merely visual or appearance-level simulation. Although several prior works are referred to as digital twins, they primarily focus on visual consistency and perform a single offline scene reconstruction, without explicitly addressing continuous state synchronization between the real world and simulation. As a result, such systems are fundamentally closer to visual simulation than to a digital twin with real-time synchronization capability. In contrast, SyncTwin is explicitly designed to continuously track and synchronize object geometry and pose, capturing dynamic changes in the environment and enabling faithful real-to-sim-to-real state consistency.

Moreover, the proposed digital twin synchronization also provides a foundation for safe real-robot reinforcement learning. By synchronizing real-world geometry into simulation, the system enables collision-aware training and execution, thereby reducing the risk associated with real-world exploration. This capability is particularly important for post-training and fine-tuning learning-based policies on physical robots.

V. CONCLUSION

We introduced SyncTwin, a digital twin framework that unifies fast RGB-only 3D reconstruction with real-time scene synchronization for safe and robust execution in dynamic, partially occluded environments. By combining learning-based reconstruction, segmentation-aware denoising, and memory-driven geometry completion, SyncTwin provides accurate object geometry and reliable grasp generation from limited visual input, enabling simulation-based planners to execute safe, collision-aware trajectories on real robots without retraining.

Our experiments demonstrate substantial improvements over existing baselines such as NVBlox, including higher obstacle-avoidance success rates, more stable behavior in dynamic environments, and improved grasp performance under single-view occlusion. These results highlight the effectiveness of

integrating fast asset generation with persistent memory and real-time synchronization for reliable real-world execution.

Looking forward, several extensions are promising. Integrating Stage I construction into Stage II synchronization would enable online asset expansion, allowing the system to incrementally acquire new objects. Extending SyncTwin beyond geometry-level synchronization to visual appearance consistency would support more realistic simulation and training of visuomotor policies. In addition, distributed or multi-GPU system designs that decouple perception, synchronization, and planning could improve responsiveness in highly dynamic scenes. Together, these directions enable adaptive and scalable digital twin synchronization for real-world robotic systems.

REFERENCES

- [1] Zhengxue Zhou, Xingyu Yang, Hao Wang, and Xuping Zhang. Digital twin with integrated robot-human/environment interaction dynamics for an industrial mobile manipulator. In *2022 International Conference on Robotics and Automation (ICRA)*, pages 5041–5047. IEEE, 2022.
- [2] Nathan Ratliff, Matt Zucker, J Andrew Bagnell, and Siddhartha Srinivasa. Chomp: Gradient optimization techniques for efficient motion planning. In *2009 IEEE international conference on robotics and automation*, pages 489–494. IEEE, 2009.
- [3] Mrinal Kalakrishnan, Sachin Chitta, Evangelos Theodorou, Peter Pastor, and Stefan Schaal. Stomp: Stochastic trajectory optimization for motion planning. In *2011 IEEE international conference on robotics and automation*, pages 4569–4574. IEEE, 2011.
- [4] John Schulman, Jonathan Ho, Alex X Lee, Ibrahim Awwal, Henry Bradlow, and Pieter Abbeel. Finding locally optimal, collision-free trajectories with sequential convex optimization. In *Robotics: science and systems*, volume 9, pages 1–10. Berlin, Germany, 2013.
- [5] Alexander Millane, Helen Oleynikova, Emilie Wirbel, Remo Steiner, Vikram Ramasamy, David Tingdahl, and Roland Siegwart. nvblox: Gpu-accelerated incremental signed distance field mapping. In *2024 IEEE International Conference on Robotics and Automation (ICRA)*, pages 2698–2705. IEEE, 2024.
- [6] Jiahui Yang, Jason Jingzhou Liu, Yulong Li, Youssef Khaky, Kenneth Shaw, and Deepak Pathak. Deep reactive policy: Learning reactive manipulator motion planning for dynamic environments. *arXiv preprint arXiv:2509.06953*, 2025.
- [7] Jianyun Xu, Song Wang, Ziqian Ni, Chunyong Hu, Sheng Yang, Jianke Zhu, and Qiang Li. Sam4d: Segment anything in camera and lidar streams. *arXiv preprint arXiv:2506.21547*, 2025.
- [8] Jianyuan Wang, Minghao Chen, Nikita Karaev, Andrea Vedaldi, Christian Rupprecht, and David Novotny. Vggt: Visual geometry grounded transformer. In *Proceedings of the Computer Vision and Pattern Recognition Conference*, pages 5294–5306, 2025.
- [9] Kenta Tanaka. cupoch – robotics with gpu computing, 2020. <https://github.com/neka-nat/cupoch>.
- [10] Mayank Mittal, Calvin Yu, Qinxi Yu, Jingzhou Liu, Nikita Rudin, David Hoeller, Jia Lin Yuan, Ritvik Singh, Yunrong Guo, Hammad Mazhar, et al. Orbit: A unified simulation framework for interactive robot learning environments. *IEEE Robotics and Automation Letters*, 8(6): 3740–3747, 2023.
- [11] Balakumar Sundaralingam, Siva Kumar Sastry Hari, Adam Fishman, Caelan Garrett, Karl Van Wyk, Valts Blukis, Alexander Millane, Helen Oleynikova, Ankur Handa, Fabio Ramos, et al. Curobo: Parallelized collision-free robot motion generation. In *2023 IEEE International Conference on Robotics and Automation (ICRA)*, pages 8112–8119. IEEE, 2023.
- [12] Richard A Newcombe, Shahram Izadi, Otmar Hilliges, David Molyneaux, David Kim, Andrew J Davison, Pushmeet Kohi, Jamie Shotton, Steve Hodges, and Andrew Fitzgibbon. Kinectfusion: Real-time dense surface mapping and tracking. In *2011 10th IEEE international symposium on mixed and augmented reality*, pages 127–136. Ieee, 2011.
- [13] Frank Steinbrücker, Jürgen Sturm, and Daniel Cremers. Real-time visual odometry from dense rgb-d images. In *2011 IEEE international conference on computer vision workshops (ICCV Workshops)*, pages 719–722. IEEE, 2011.
- [14] Mingsong Dou, Li Guan, Jan-Michael Frahm, and Henry Fuchs. Exploring high-level plane primitives for indoor 3d reconstruction with a hand-held rgb-d camera. In *Asian Conference on Computer Vision*, pages 94–108. Springer, 2012.
- [15] Angela Dai, Matthias Nießner, Michael Zollhöfer, Shahram Izadi, and Christian Theobalt. Bundlefusion: Real-time globally consistent 3d reconstruction using on-the-fly surface reintegration. *ACM Transactions on Graphics (ToG)*, 36(4):1, 2017.
- [16] John Oliensis. A critique of structure-from-motion algorithms. *Computer Vision and Image Understanding*, 80(2):172–214, 2000.
- [17] Johannes L Schonberger and Jan-Michael Frahm. Structure-from-motion revisited. In *Proceedings of the IEEE conference on computer vision and pattern recognition*, pages 4104–4113, 2016.
- [18] Onur Özyeşil, Vladislav Voroninski, Ronen Basri, and Amit Singer. A survey of structure from motion*. *Acta Numerica*, 26:305–364, 2017.
- [19] Richard Hartley and Andrew Zisserman. *Multiple view geometry in computer vision*. Cambridge university press, 2003.
- [20] Steven M Seitz, Brian Curless, James Diebel, Daniel Scharstein, and Richard Szeliski. A comparison and evaluation of multi-view stereo reconstruction algorithms. In *2006 IEEE computer society conference on computer vision and pattern recognition (CVPR'06)*, volume 1, pages 519–528. IEEE, 2006.

- [21] Yasutaka Furukawa and Jean Ponce. Accurate, dense, and robust multiview stereopsis. *IEEE transactions on pattern analysis and machine intelligence*, 32(8):1362–1376, 2009.
- [22] Silvano Galliani, Katrin Lasinger, and Konrad Schindler. Massively parallel multiview stereopsis by surface normal diffusion. In *Proceedings of the IEEE international conference on computer vision*, pages 873–881, 2015.
- [23] Yao Yao, Zixin Luo, Shiwei Li, Tian Fang, and Long Quan. Mvsnet: Depth inference for unstructured multi-view stereo. In *Proceedings of the European conference on computer vision (ECCV)*, pages 767–783, 2018.
- [24] Ben Mildenhall, Pratul P Srinivasan, Matthew Tancik, Jonathan T Barron, Ravi Ramamoorthi, and Ren Ng. Nerf: Representing scenes as neural radiance fields for view synthesis. *Communications of the ACM*, 65(1):99–106, 2021.
- [25] Bernhard Kerbl, Georgios Kopanas, Thomas Leimkühler, and George Drettakis. 3d gaussian splatting for real-time radiance field rendering. *ACM Trans. Graph.*, 42(4):139–1, 2023.
- [26] Yuchen Zhou, Jiayuan Gu, Tung Yen Chiang, Fanbo Xiang, and Hao Su. Point-sam: Promptable 3d segmentation model for point clouds. *arXiv preprint arXiv:2406.17741*, 2024.
- [27] Weiyue Wang, Ronald Yu, Qiangui Huang, and Ulrich Neumann. Sgpn: Similarity group proposal network for 3d point cloud instance segmentation. In *Proceedings of the IEEE conference on computer vision and pattern recognition*, pages 2569–2578, 2018.
- [28] Li Jiang, Hengshuang Zhao, Shaoshuai Shi, Shu Liu, Chi-Wing Fu, and Jiaya Jia. Pointgroup: Dual-set point grouping for 3d instance segmentation. In *Proceedings of the IEEE/CVF conference on computer vision and pattern recognition*, pages 4867–4876, 2020.
- [29] Martin Runz, Maud Buffier, and Lourdes Agapito. Mask-fusion: Real-time recognition, tracking and reconstruction of multiple moving objects. In *2018 IEEE international symposium on mixed and augmented reality (ISMAR)*, pages 10–20. IEEE, 2018.
- [30] John McCormac, Ronald Clark, Michael Bloesch, Andrew Davison, and Stefan Leutenegger. Fusion++: Volumetric object-level slam. In *2018 international conference on 3D vision (3DV)*, pages 32–41. IEEE, 2018.
- [31] Dingyuan Zhang, Dingkan Liang, Hongcheng Yang, Zhikang Zou, Xiaoqing Ye, Zhe Liu, and Xiang Bai. Sam3d: Zero-shot 3d object detection via segment anything model. *arXiv preprint arXiv:2306.02245*, 2023.
- [32] Mutian Xu, Xingyilang Yin, Lingteng Qiu, Yang Liu, Xin Tong, and Xiaoguang Han. Sampro3d: Locating sam prompts in 3d for zero-shot instance segmentation. In *2025 International Conference on 3D Vision (3DV)*, pages 1222–1232. IEEE, 2025.
- [33] Mohamed El Amine Boudjoghra, Angela Dai, Jean Lahoud, Hisham Cholakkal, Rao Muhammad Anwer, Salman Khan, and Fahad Shahbaz Khan. Open-yolo 3d: Towards fast and accurate open-vocabulary 3d instance segmentation. *arXiv preprint arXiv:2406.02548*, 2024.
- [34] Yevgen Chebotar, Ankur Handa, Viktor Makoviychuk, Miles Macklin, Jan Issac, Nathan Ratliff, and Dieter Fox. Closing the sim-to-real loop: Adapting simulation randomization with real world experience. In *2019 International Conference on Robotics and Automation (ICRA)*, pages 8973–8979. IEEE, 2019.
- [35] Yuxuan Wu, Lei Pan, Wenhua Wu, Guangming Wang, Yanzi Miao, Fan Xu, and Hesheng Wang. Rl-gsbridge: 3d gaussian splatting based real2sim2real method for robotic manipulation learning. In *2025 IEEE International Conference on Robotics and Automation (ICRA)*, pages 192–198. IEEE, 2025.
- [36] Haoqi Yuan, Ziyue Huang, Ye Wang, Chuan Mao, Chaoyi Xu, and Zongqing Lu. Demograsp: Universal dexterous grasping from a single demonstration. *arXiv preprint arXiv:2509.22149*, 2025.
- [37] Marcel Torne, Anthony Simeonov, Zechu Li, April Chan, Tao Chen, Abhishek Gupta, and Pulkrit Agrawal. Reconciling reality through simulation: A real-to-sim-to-real approach for robust manipulation. *arXiv preprint arXiv:2403.03949*, 2024.
- [38] Yao Mu, Tianxing Chen, Zanxin Chen, Shijia Peng, Zhiqian Lan, Zeyu Gao, Zhixuan Liang, Qiaojun Yu, Yude Zou, Mingkun Xu, et al. Robotwin: Dual-arm robot benchmark with generative digital twins. In *Proceedings of the Computer Vision and Pattern Recognition Conference*, pages 27649–27660, 2025.
- [39] Pushkal Katara, Zhou Xian, and Katerina Fragkiadaki. Gen2sim: Scaling up robot learning in simulation with generative models. In *2024 IEEE International Conference on Robotics and Automation (ICRA)*, pages 6672–6679. IEEE, 2024.
- [40] Chuanruo Ning, Kuan Fang, and Wei-Chiu Ma. Prompting with the future: Open-world model predictive control with interactive digital twins. *arXiv preprint arXiv:2506.13761*, 2025.
- [41] Yuzhu Sun, Mien Van, Stephen McIlvanna, Nguyen Minh Nhat, Kabirat Olayemi, Jack Close, and Seán McLoone. Digital twin-driven reinforcement learning for obstacle avoidance in robot manipulators: A self-improving online training framework. *arXiv preprint arXiv:2403.13090*, 2024.
- [42] Ioan A Sucas, Mark Moll, and Lydia E Kavraki. The open motion planning library. *IEEE Robotics & Automation Magazine*, 19(4):72–82, 2012.
- [43] Sertac Karaman and Emilio Frazzoli. Sampling-based algorithms for optimal motion planning. *The international journal of robotics research*, 30(7):846–894, 2011.
- [44] Lukas Brunke, Yanni Zhang, Ralf Römer, Jack Naimier, Nikola Staykov, Siqi Zhou, and Angela P Schoellig. Semantically safe robot manipulation: From semantic scene understanding to motion safeguards. *IEEE Robotics and Automation Letters*, 2025.
- [45] Kensuke Nakamura, Lasse Peters, and Andrea Ba-

- jcsy. Generalizing safety beyond collision-avoidance via latent-space reachability analysis. *arXiv preprint arXiv:2502.00935*, 2025.
- [46] Arpit Bahety, Arnav Balaji, Ben Abbatematteo, and Roberto Martín-Martín. Safemimic: Towards safe and autonomous human-to-robot imitation for mobile manipulation. *arXiv preprint arXiv:2506.15847*, 2025.
- [47] Lai Wei, Jiahua Ma, Yibo Hu, and Ruimao Zhang. Ensuring force safety in vision-guided robotic manipulation via implicit tactile calibration. *arXiv preprint arXiv:2412.10349*, 2024.
- [48] Jeon Ho Kang, Sagar Joshi, Ruopeng Huang, and Satyandra K Gupta. Robotic compliant object prying using diffusion policy guided by vision and force observations. *IEEE Robotics and Automation Letters*, 2025.
- [49] Murtaza Dalal, Jiahui Yang, Russell Mendonca, Youssef Khaky, Ruslan Salakhutdinov, and Deepak Pathak. Neural mp: A generalist neural motion planner. *arXiv preprint arXiv:2409.05864*, 2024.
- [50] Adam Fishman, Adithyavairavan Murali, Clemens Eppner, Bryan Peele, Byron Boots, and Dieter Fox. Motion policy networks. In *conference on Robot Learning*, pages 967–977. PMLR, 2023.
- [51] Álvaro González. Measurement of areas on a sphere using fibonacci and latitude–longitude lattices. *Mathematical geosciences*, 42(1):49–64, 2010.
- [52] Gene H Golub and Christian Reinsch. Singular value decomposition and least squares solutions. In *Linear algebra*, pages 134–151. Springer, 1971.
- [53] Martin A Fischler and Robert C Bolles. Random sample consensus: a paradigm for model fitting with applications to image analysis and automated cartography. *Communications of the ACM*, 24(6):381–395, 1981.
- [54] Gabriel Taubin. A signal processing approach to fair surface design. In *Proceedings of the 22nd annual conference on Computer graphics and interactive techniques*, pages 351–358, 1995.
- [55] Jaesik Park, Qian-Yi Zhou, and Vladlen Koltun. Colored point cloud registration revisited. In *Proceedings of the IEEE international conference on computer vision*, pages 143–152, 2017.
- [56] Xinyue Wei, Minghua Liu, Zhan Ling, and Hao Su. Approximate convex decomposition for 3d meshes with collision-aware concavity and tree search. *ACM Transactions on Graphics (TOG)*, 41(4):1–18, 2022.
- [57] Matthew Tancik, Ethan Weber, Evonne Ng, Ruilong Li, Brent Yi, Terrance Wang, Alexander Kristoffersen, Jake Austin, Kamyar Salahi, Abhik Ahuja, et al. Nerfstudio: A modular framework for neural radiance field development. In *ACM SIGGRAPH 2023 conference proceedings*, pages 1–12, 2023.
- [58] Adithyavairavan Murali, Balakumar Sundaralingam, Yu-Wei Chao, Wentao Yuan, Jun Yamada, Mark Carlson, Fabio Ramos, Stan Birchfield, Dieter Fox, and Clemens Eppner. Graspgen: A diffusion-based framework for 6-dof grasping with on-generator training. *arXiv preprint* *arXiv:2507.13097*, 2025.

APPENDIX A
DENOISING ALGORITHMS DETAILS

1) *Robust Center Estimation.*: Given a point cloud $\mathcal{P} = \{\mathbf{p}_i \in \mathbb{R}^3\}$, we compute a robust geometric center \mathbf{c} to reduce bias from uneven sampling:

$$\mathbf{c} = \text{mean}(\mathcal{P}). \quad (3)$$

2) *Directional Discretization via Fibonacci Sphere.*: We uniformly sample K directions $\{\mathbf{d}_i\}_{i=1}^K$ on the unit sphere using the Fibonacci spiral:

$$\theta_i = \arccos\left(1 - \frac{2i}{K}\right), \quad \phi_i = \pi(1 + \sqrt{5})i, \quad (4)$$

$$\mathbf{d}_i = [\sin \theta_i \cos \phi_i, \sin \theta_i \sin \phi_i, \cos \theta_i]^\top. \quad (5)$$

These directions form a discrete spherical domain \mathcal{D} for ray-wise accumulation.

3) *Point-to-Bucket Assignment.*: Each point defines a normalized direction from the center:

$$\hat{\mathbf{v}}_i = \frac{\mathbf{p}_i - \mathbf{c}}{\|\mathbf{p}_i - \mathbf{c}\|}. \quad (6)$$

A point is assigned to direction bucket \mathbf{d}_j if the angular deviation satisfies:

$$\hat{\mathbf{v}}_i \cdot \mathbf{d}_j \geq \cos(\theta_{\text{tolerance}}), \quad (7)$$

where θ_{tol} is the angular tolerance.

4) *Progressive Sphere Expansion.*: We iteratively expand a sphere centered at \mathbf{c} with radius r_t :

$$r_{t+1} = r_t + \Delta r. \quad (8)$$

A direction \mathbf{d}_j is marked as *hit* when any assigned point enters the sphere:

$$r_{\min}(j) = \min_{i \in \text{bucket } j} \|\mathbf{p}_i - \mathbf{c}\|. \quad (9)$$

Unhit directions form a binary mask $\mathcal{U}_t = \{j \mid \text{hit}(j) = 0\}$. Connected components on the spherical adjacency graph are extracted to identify large uncovered regions. Stability is detected when the largest unhit component remains consistent over multiple iterations:

$$\frac{\max(|\mathcal{C}_{\max}^{(t-k:t)}|) - \min(|\mathcal{C}_{\max}^{(t-k:t)}|)}{\max(|\mathcal{C}_{\max}^{(t-k:t)}|)} < \epsilon. \quad (10)$$

5) *Boundary and Rim Extraction.*: Boundary buckets are defined as unhit directions adjacent to hit ones:

$$\mathcal{B} = \{j \in \mathcal{U} \mid \exists k \in \mathcal{N}(j), \text{hit}(k) = 1\}. \quad (11)$$

For each boundary direction \mathbf{d}_j , the farthest point within angular tolerance is selected as a rim point:

$$\mathbf{p}_j^* = \arg \max_{\mathbf{p}_i \in \mathcal{P}} \|\mathbf{p}_i - \mathbf{c}\|, \quad \text{s.t. } \hat{\mathbf{v}}_i \cdot \mathbf{d}_j \geq \cos(\theta_{\text{tol}}). \quad (12)$$

If no candidate is found, finer sub-buckets around \mathbf{d}_j are generated to refine sampling.

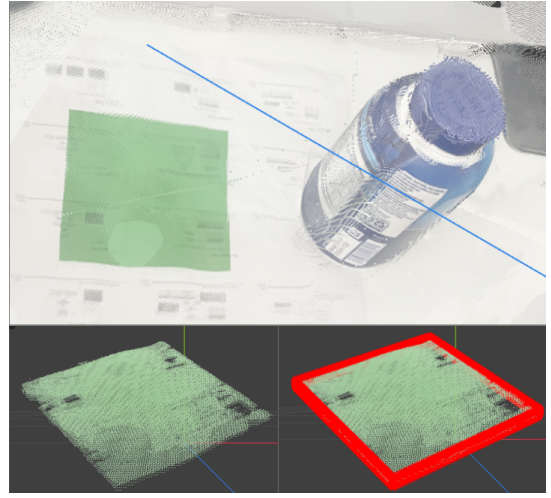


Fig. 11: **Green cube-based scale estimation.** The top image shows the whole reconstructed point cloud. The bottom illustrates the isolated cube points and the fitted red bounding box. By measuring the cube’s average edge length in VGGT-normalized coordinates and comparing it to the known real-world cube size (e.g., 0.1 m), the scale factor between VGGT coordinates and real-world metric space is computed.

6) *Opening Axis and Plane Fitting.*: The principal opening direction is computed by averaging the largest unhit component:

$$\mathbf{n}_{\text{open}} = \frac{\sum_{j \in \mathcal{C}_{\max}} \mathbf{d}_j}{\left\| \sum_{j \in \mathcal{C}_{\max}} \mathbf{d}_j \right\|}. \quad (13)$$

Rim points $\{\mathbf{p}_j^*\}$ are used to fit an opening plane via SVD, providing a visualizable orientation and boundary.

APPENDIX B
GREEN CUBE-BASED SCALE ESTIMATION ALGORITHM

To determine the scale between VGGT-normalized coordinates and real-world measurements, we identify a green-colored reference cube embedded in the scene. The process involves the following steps:

1) *Point Cloud and Color Extraction.*: The GLB file is loaded, and 3D point coordinates along with RGB vertex colors are extracted from the embedded mesh.

2) *Green Point Detection.*: We employ multiple criteria to detect green points:

- Channel thresholding: strong green with low red/blue values.
- Channel dominance ratio: green significantly dominates red and blue.
- HSV filtering: hue and saturation conditions for green.
- PCA-based refinement and outlier filtering.

Among several detection masks, the method yielding a reasonable number of points (1000–50000) is selected to ensure tight coverage of the cube. The result is shown in Fig. 11.



Fig. 12: Segmented 3D point clouds in our experiments.

3) *Cube Dimension Analysis.*: The bounding box of detected green points is computed to estimate the cube dimensions. A refined analysis using PCA is then applied to:

- Extract principal directions.
- Project points onto the main 2D plane.
- Compute four edge lengths of the square face from percentiles.

4) *Scale Factor Estimation.*: The average of the four edge lengths (in VGGT units) is compared with the known real-world cube size (e.g., 0.1 m) to compute the scale factor:

$$\text{Scale Factor} = \frac{\text{Real Cube Size}}{\text{Average Measured Length}}$$

This algorithm provides a robust estimation of coordinate scale using only geometric and color cues, without requiring prior calibration.

APPENDIX C 3D ASSET VISUALIZATION

We construct object assets using RGB images captured by a standard camera (e.g., a mobile phone), rather than relying on multiple depth sensors, for several practical reasons.

First, RGB cameras are low-cost and widely available, allowing asset acquisition to be performed easily using commodity devices such as smartphones. Second, our system already employs a single RealSense camera that is fixed in the environment for online perception and tracking.

Using this depth camera for asset construction would require moving it around the scene to capture multiple viewpoints, followed by repeated extrinsic calibration each time the camera is re-mounted. In practice, this calibration process is time-consuming and cumbersome, especially when assets need to be constructed for different environments. By contrast, using a handheld RGB camera avoids repeated extrinsic calibration entirely, enabling flexible multi-view data capture by simply walking around the scene. This design choice significantly reduces the overhead of asset acquisition and improves deployability in real-world settings.

Finally, while some prior works rely on fixed cameras and rotate the target object during reconstruction, this assumption does not hold in many realistic scenarios. For large objects or static environments such as tables, shelves, or cabinets, rotating the object is infeasible. Our RGB-based asset construction strategy naturally supports such settings by allowing viewpoint changes without requiring object manipulation.

Figure 12 shows the reconstructed assets used in our experiments, including a chip can, a cookie box, a Coke can, a spam can, a regular box, and a ketchup bottle. These objects have relatively regular and mostly convex shapes, making them representative of common household items.

We also include more irregular objects, such as the toy bear and the cup with a thin handle. Despite their asymmetric geometry and concave regions, the reconstruction pipeline can recover complete object meshes and segment them cleanly from the background, providing reliable assets for downstream synchronization and planning.

APPENDIX D TIPS FOR PRACTICAL IMPLEMENTATION

We summarize several engineering considerations that are important for reproducing SyncTwin in practice. These remarks are not essential to the core algorithmic contributions, but help avoid common pitfalls during system integration. To preserve anonymity during the review process, the implementation will be considered for full release after the review cycle.

1) *VGGT Extrinsics Are Not Stored in the GLB File:* VGGT predicts per-image camera poses, but these extrinsics are *not* embedded in the exported GLB mesh. Instead, they are stored in the accompanying `predictions.npz` file and must be explicitly loaded for projection-based segmentation.

2) *Mask Ordering for Projection Segmentation.*: When projecting masks onto the reconstructed point cloud, the ordering of masks must match the ordering of input images and camera poses. For improved efficiency, one may first down-sample the global point cloud before performing projection-based segmentation.

3) *Asset Centering for Consistent Pose Alignment:* ICP alignment uses 4×4 homogeneous matrices, whereas Isaac Sim stores object poses using quaternions. To maintain one-to-one correspondence, each 3D asset must be centered at its geometric centroid; otherwise, rotation pivots differ between ICP and the simulator. Note also that Isaac Sim uses the quaternion ordering (w, x, y, z) rather than (x, y, z, w) .

4) *Distinguishing camera_optical from RealSense Physical Extrinsic:* Frames labeled `camera_optical` follow the optical-frame convention and are not identical to the physical RealSense camera frames. Care must be taken when converting between real-world and simulator coordinate systems.

5) *Point Cloud Tracking and RealSense Reset Behavior:* Our implementation resolves the issue where restarting the tracking node may cause hardware resource conflicts. If users still encounter RealSense access errors, replugging the device typically resolves the problem. When storing per-vertex color, ensure correct RGB ordering, as OpenCV may need BGR while Open3D is RGB.

6) *Using GraspGen with SyncTwin:* GraspGen requires converting point clouds into its JSON-based format before inference. When deployed via Docker, users must ensure that communication ports are properly exposed for message passing between SyncTwin modules.

7) *NVblox Filtering Range Adjustment:* The default NVBlox depth-integration range may be too small for table-top scenes, potentially causing incomplete or missing geometry. Increasing the truncation or bounding-volume range is recommended for robotic manipulation tasks.

8) *Synchronization Requirements for cuRobo:* cuRobo planning depends on strict real-to-sim synchronization. If the simulated state is not updated in sync with the real environment, planning may diverge and lead to execution failure. Maintaining accurate digital-twin updates is essential for safe and stable planning.